Preprints of the 21st IFAC World Congress (Virtual)
Berlin, Germany, July 12-17, 2020

Flight control of flapping-wing robot with three paired direct-driven piezoelectric actuators

T. Jimbo * **T. Ozaki** * **Y. Amano** * **K. Fujimoto** **

* *Strategic Research Division, Toyota Central R&D Labs., Inc., Nagakute, Aichi 480-1192, Japan (e-mail: t-jmb@mosk.tytlabs.co.jp, ozaki@mosk.tytlabs.co.jp, e0738@mosk.tytlabs.co.jp).*
** *Department of Aeronautics and Astronautics, Kyoto University, Kyotodaigaku-katsura, Nishikyo Ward, Kyoto, Kyoto 615-8540, Japan, (e-mail: k.fujimoto@ieee.org)*

Abstract:
To realize safe mobile sensing in spaces around people, a flapping-wing robot with a weight of 1.15 g, wingspan of 115 mm, and three paired actuators is designed and fabricated in this study. The paired-wing actuators enable the suppression of wing–body and wing–wing coupling vibrations, as well as enhance the lift force. A model-based design of a stable flight controller was considered, where the lift force was assumed to work at an acting point on spatio-temporal average. Furthermore, an adaptive control law was employed for parameters that could not be measured. The effectiveness of the proposed controller was demonstrated through flight experiments.

Keywords: Flying robot, Flapping wing, Flight control, Adaptive control.

1. INTRODUCTION

Mobile sensors and their networks have been widely used in various applications such as monitoring and inspection. They exhibit high mobility and can be used for efficiently exploring wide spaces such as farms, roads, buildings, and bridges. In the future, sensing will be required around people in spaces, such as living spaces. Unmanned aerial vehicles (UAVs), such as quadrotors are some of the most common mobile sensors, and UAVs of various sizes and weights have been commercialized. The lift force for UAVs is based on the rotation of multiple propellers; thus, in spaces close to people, UAVs pose a risk of injury via collisions.

Bioinspired flapping-wing micro aerial vehicles (FW-MAVs) have been actively studied. The FW-MAVs exhibit interesting features, such as high maneuverability and efficiency, which are inherent in insects and birds. Numerous studies on the dynamic modeling, stability, and control of FW-MAVs have been reported, as summarized by Orlowski and Girard (2012). Apparently, the estimation of the lift force generated by wings is important for controlled flight; therefore, various blade–element/quasi-steady aerodynamic models have been proposed. Ozaki and Hamaguchi (2018b) studied the dynamic model of the flapping motion by considering passive wing rotation explained in Dickinson et al. (1999). However, it is difficult to estimate the varying lift force generated during the flapping motion of the wing, owing to imprecise estimations of the instantaneous aerodynamic force, which cannot be measured accurately. Manufacturing errors and variation in system properties over time, which cannot be measured either, complicate the estimation. Furthermore, because the instantaneous lift force during the flapping motion of the wing can also not be measured accurately, system identification is not feasible.

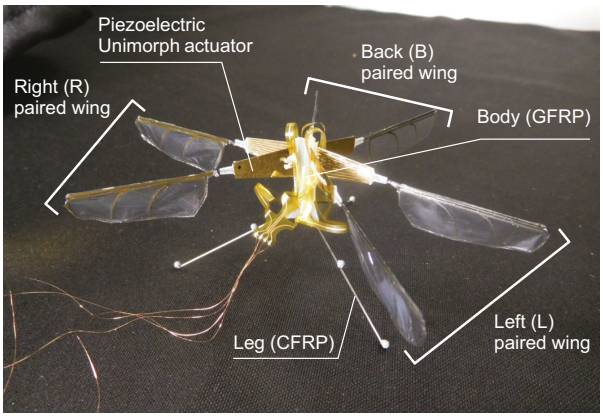

Fig. 1. Newly developed flapping-wing robot with three paired wings, six piezoelectric actuators, glass-fiber-reinforced plastic body, and three carbon-fiber-reinforced plastic legs. Wingspan is 115 mm, and the weight is 1150 mg.

We previously explored direct-driven piezoelectric actuators without a displacement-amplifying structure because of the simplicity thereof. Ozaki and Hamaguchi (2018c) fabricated a direct-driven flapping-wing with a piezoelectric unimorph actuator. This study proposes a modeling and flight controller for a newly developed FW-MAV with three paired wings composed of the unimorph actuators

(Fig. 1). Herein, we assume the lift force to work at an acting point on spatio-temporal average. The modeling error is defined by the misalignment of the force frame related to the body frame, and the corresponding unknown parameters are derived as the offset force and torques. Furthermore, an adaptive control law is employed because these parameters cannot be measured. The major contributions of this study are summarized below:

- A novel FW-MAV with three paired wings is fabricated. The wing is driven by two piezoelectric unimorph actuators with no transmission.
- The FW-MAV is modeled with unknown offset forces.
- A flight controller for the FW-MAV is designed, and controlled flight is demonstrated.

The remainder of this paper is organized as follows. Section 2 describes the related work conducted on the development of various types of FW-MAVs as well as our previous work. The newly developed flapping-wing robot is described, along with the performance of the flapping-wing actuator, in Section 3. In Section 4, the dynamic model of the robot is introduced, and Section 5 describes the flight controller, which is experimentally evaluated in Section 6. Finally, Section 7 concludes the paper.

2. RELATED WORK

FW-MAVs require certain mechanisms to be implemented to enable generation of the flapping motion. Various approaches have been proposed for flapping-wing actuation, such as the use of electrical motors, piezoelectric materials, electro-active polymers, and shape memory alloys. Recently, electromagnetic and piezoelectric mechanisms have shown promising results. Electrical motors are reliable and suitable for aircraft heavier than several grams, considering their efficiency. Motor-driven flapping-wing robots must generate fast reciprocating motion from the rotating motion. In de Croon et al. (2009) and Keennon et al. (2012), transmission mechanisms with parts such as gears, crankshaft, belts, and pulleys were proposed. However, an FW-MAV with direct-driven DC motors has recently been proposed in Azhar et al. (2013), Hines et al. (2014), and Zhang et al. (2017), but the types that could realize liftoff were heavier than a few grams.

Piezoelectric actuation can directly generate the reciprocating motion of wings, and it is suitable for very small and lightweight FW-MAVs because of its high power density. Furthermore, such actuation does not require complex transmission mechanisms, which is advantageous for manufacturing processes. However, piezoelectric actuators must generate a large flapping motion from the small displacement of the piezoelectric plate. Accordingly, various FW-MAVs with different displacement-amplifying structures have been studied. Wood (2008) developed an insect-scale MAV (with a wingspan of 3.5 cm and weight of 80 mg) with piezoelectric bimorph actuators and a lever mechanism. A flight controller has been developed and tethered flight has been demonstrated by Ma et al. (2013) and Chirarattananon et al. (2013). In addition, Mateti et al. (2012) and Nguyen et al. (2008) proposed FW-MAVs driven by piezoelectric bimorph actuators employing a slider–rocker mechanism and a piezoelectric unimorph actuator with a four-bar linkage mechanism, respectively. However, these are complicated mechanisms that are not desirable, considering that they can increase the manufacturing cost. On the contrary, Bronson et al. (2009) proposed a piezoelectric unimorph actuator with no transmission; however, lift-force generation and controlled flight were not demonstrated.

Piezoelectric unimorph actuators fabricated in Ozaki and Hamaguchi (2018c) was evaluated in terms of the stroke amplitude, lift force, and power consumption using finite element analysis (FEA) and measurement experiments. As a result, the piezoelectric material was selected. Ozaki and Hamaguchi (2018a) also developed an FW-MAV with two flapping wings (with a wingspan of 114 mm and weight of 598 mg). The lift force was evaluated via experiments on a single wing as well as on an assembled robot, and we further demonstrated the takeoff of the two-wing robot under a 1-DoF constraint.

3. PROPOSED ROBOT

3.1 Direct-driven Flapping-wing Actuator

Figure 2 shows the direct-driven flapping-wing actuator fabricated by us. The actuator consists only of a wing and a piezoelectric unimorph plate. It has a simple structure because it does not employ any transmission. The passive wing rotation during the stroke motion plays a key role in generating the lift force. Therefore, a hinge structure using a polyimide flexible torsional beam was placed near the top edge of the wing. To produce a large deformation of the unimorph actuator, the single-crystal $Pb(In_{1/2}Nb_{1/2})O_3$–$Pb(Mg_{1/3}Nb_{2/3})O_3$–$PbTiO_3$ (PIN–PMN–PT) was selected. The PIN–PMN–PT is excellent in terms of lift force-to-power efficiency and lift force-to-weight ratio. When a sinusoidal-wave voltage at a certain frequency is applied to the plate, the plate is bent by the piezoelectric effect.

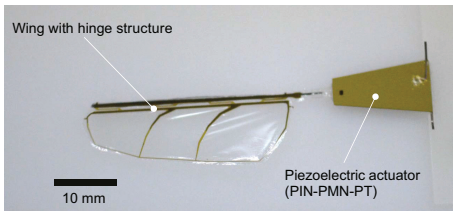

Fig. 2. Photograph of direct-driven flapping-wing actuator.

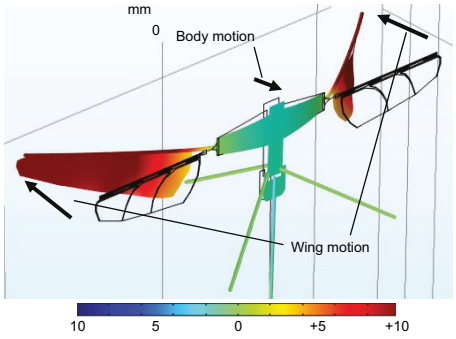

Fig. 3. Shape deformation of direct-driven two-wing robot.

3.2 Three-paired-wing Robot

Our preliminary experiments show that the lift force of a conventional two-wing robot is significantly lesser than that of a wing having its support end fixed to the ground. Figure 3 shows the shape deformation of the two-wing robot, which was calculated using FEA. Because the body moves in a direction opposite to that of the wing stroke motion, the velocity of the wings decreases, causing lift-force reduction.

To suppress the wing–body and wing–wing coupling effect (Fig. 1), two wings are paired, and three pairs are assembled in the robot body.

4. MODELING

4.1 Performance of Single Actuator

Ozaki and Hamaguchi (2018b) proposed a blade–element /quasi–steady aerodynamic model as a flapping-wing actuator considering the flapping motion and passive wing rotation (Fig. 2). The lift force varies during the flapping motion because of the aerodynamic force depending on the velocity of the wing-stroke angle, passive wing rotational angle, and velocity. The difficulty in modeling presents in terms of the imprecise estimations of the aerodynamic force.

Therefore, in this study, the relationship between the voltage amplitude and the lift force is directly modeled based on the values measured using the experimental setup in Ozaki and Hamaguchi (2018b). In other words, the lift force is assumed to work at an acting point on spatio-temporal average.

Figures 4(a) and 4(b) show the experimental results of the frequency responses of the stroke amplitude and lift force, respectively, for the six samples fabricated using the same design at a voltage amplitude of 100V. In the measurement experiment, a single actuator is fixed rigidly. The dynamics of the wing position can be approximated by a second-order system. The wing stroke in Fig. 4(a) is the amplitude of steady vibration forced by an external sinusoidal voltage wave. The resonant frequency and damping ratio of the wing position are identified from Fig. 4(a). The resonant frequency is extracted, and the voltage is driven at this frequency.

The velocity of the wing is proportional to the wing-stroke amplitude. Because the aerodynamic force increases with the velocity, the lift force is proportionally related to the stroke amplitude. Figure 4 indicates that both the stroke amplitudes and the lift forces are maximum at a resonant frequency of approximately 115 Hz. At the resonant frequency, the average lift forces increase linearly with the increase in voltage amplitude (Fig. 5).

4.2 Lift-force Model

Figure 6 shows the lift forces of the robot with three paired-wing actuators. Here, the same voltage amplitudes are applied to the two wings within a single actuator. Compared with the result for the single wing in Fig. 5,

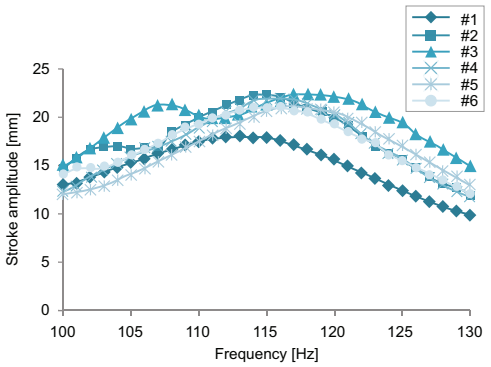

(a)

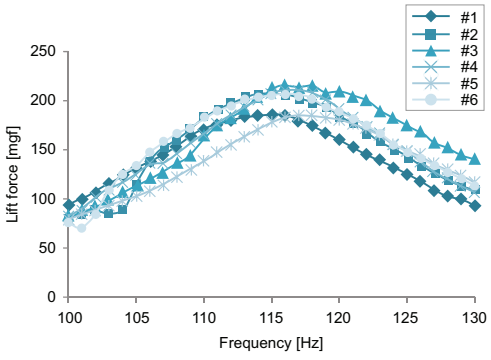

(b)

Fig. 4. Frequency responses of (a) wing-stroke amplitude and (b) lift force for rigidly fixed single actuators at a voltage amplitude of 100 V.

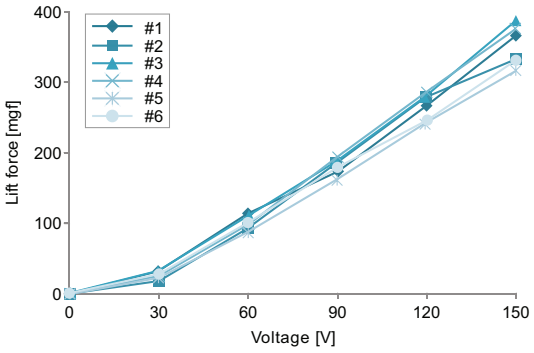

Fig. 5. Lift force of rigidly fixed single actuators depending on the voltage amplitude at a driving frequency of 115 Hz.

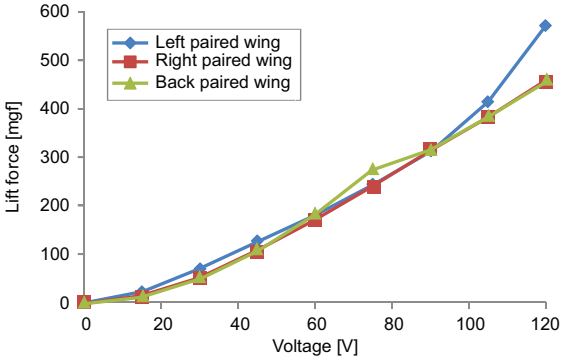

Fig. 6. Lift force of paired-wing actuators assembled in the body at a driving frequency of 115 Hz.

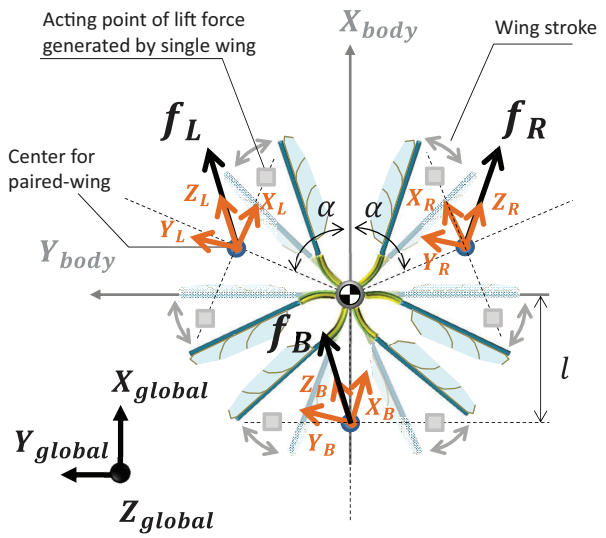

Fig. 7. Lift forces at acting points.

the lift force generated by the actuator with two wings was almost twice the lift force generated by the rigidly fixed single actuator.

From Fig. 6, the relationship between the demanded lift force f_d in the steady state and the voltage amplitude V is approximated by the following linear equation around the voltage at which the robot supports its own weight for $i \in \{L, R, B\}$:

$$f_{d,i} = a_i V_i - b_i, \tag{1}$$

where a_i and b_i are positive constant values.

Furthermore, because the transient response of the wing stroke to the voltage amplitude exhibits a lag in relation to the dynamics of the wing position, the average lift force f_i can be approximated by the following first-order lag system:

$$\dot{f}_i = \frac{1}{T}(f_{d,i} - f_i), \tag{2}$$

where $T(>0)$ is a time constant, which can be estimated from the dynamics of the wing position, and is the frequency response of the stroke amplitude, as shown in Fig. 4(a). Note that the lift force oscillates depending on the reciprocating motion of the wing. In this study, the oscillation component is not considered.

4.3 Offset Lift Force and Torque

The direction of lift force of paired-wing is not necessarily along the z-axis of the body frame (vertically upward) because of effects such as unmodeled aerodynamic effect, manufacturing error, and variation in system properties over time. In Fig. 7, each force frame is defined to consider each misalignment. The lift force of each wing is assumed to work at an acting point on spatio-temporal average. In this study, for each paired-wing actuator, the torque center of the corresponding two acting points is defined as the lift-force center.

Using the rotation matrix $\boldsymbol{R}_i$ between the force frame i and the body frame at the gravity center, f_i in the force frame i is translated to that in the body frame as follows for $i \in \{L, R, B\}$:

$$F_i = \boldsymbol{R}_i \begin{bmatrix} 0 \\ 0 \\ f_i \end{bmatrix} = \begin{bmatrix} R_{i,13} f_i \\ R_{i,23} f_i \\ R_{i,33} f_i \end{bmatrix}, \tag{3}$$

where $R_{i,33} = \cos(\epsilon_{x,i})\cos(\epsilon_{y,i})$, with $\epsilon_{x,i}$ and $\epsilon_{y,i}$ being the misalignment angles of the lift force from the Z_i axis. Roll and pitch torques are generated by the third element in (3) as follows:

$$F_{i3} = R_{i,33} f_i = f_i - \delta_i, \tag{4}$$

where $\delta_i (= (1 - R_{i,33}) f_i)$ depends on f_i. Note that, in this study, δ_i is assumed to be constant around the lift force required for the robot to support its own weight.

The lift force f_b, roll torque τ_{b1}, and pitch torque τ_{b2} in the body frame are derived from the geometrical relationship as follows:

$$\begin{bmatrix} f_b \\ \tau_{b1} \\ \tau_{b2} \end{bmatrix} = M \begin{bmatrix} F_{L3} \\ F_{R3} \\ F_{B3} \end{bmatrix}, \tag{5}$$

where the mixing matrix M is given by

$$M = \begin{bmatrix} 1 & 1 & 1 \\ l\sin\alpha & -l\sin\alpha & 0 \\ -l\cos\alpha & -l\cos\alpha & l \end{bmatrix}. \tag{6}$$

Here, l is the distance between the gravity center and lift-force center, and α is the half angle between the left and right paired wings. Note that, because the yaw torque of the body cannot be generated, the yaw angle is not controlled in this study. Furthermore, l cannot be measured and estimated accurately, and α depicts a manufacturing error.

From (4) and (5), the force and torques acting on the robot body are given by

$$f_b = f - f_o, \tag{7}$$
$$\tau_{b1} = \tau_1 - \tau_{o1}, \tag{8}$$
$$\tau_{b2} = \tau_2 - \tau_{o2}, \tag{9}$$

where

$$\begin{aligned} f &= f_L + f_R + f_B, \\ \tau_1 &= l\sin\alpha(f_L - f_R), \\ \tau_2 &= -l\cos\alpha(f_L + f_R) + l f_B, \end{aligned}$$

and the offset force and torques are given by

$$f_o = \delta_L + \delta_R + \delta_B, \tag{10}$$
$$\tau_{o1} = l\sin\alpha(\delta_L - \delta_R), \tag{11}$$
$$\tau_{o2} = -l\cos\alpha(\delta_L + \delta_R) + l\delta_B. \tag{12}$$

These offsets are defined as unknown parameters because the robot is small and the misalignment angle δ_i is not measured.

4.4 Flight Dynamics

Consider the rigid-body model of the robot shown in Fig. 1. Considering (2) and (7), the dynamics in the vertical direction, i.e., z-axis, is represented by

$$m\ddot{z} = (\cos\phi\cos\theta)f_b - mg \approx f - f_o - mg, \quad (13)$$

$$\dot{f} = \frac{1}{T}(f_d - f), \quad (14)$$

where m is the mass of the robot, f_d is the demanded lift force, and ϕ and θ are the roll and pitch angles, respectively.

Next, considering (2), (8), and (9), the rotational dynamics is described by

$$J\dot{\omega} = \tau_b - F(\omega) = \tau - \tau_o - F(\omega), \quad (15)$$

$$\dot{\tau} = \frac{1}{T}(\tau_d - \tau), \quad (16)$$

where $\omega = [\omega_1, \omega_2, \omega_3]^\top$ is the angular velocity of the body. Kinematically, the angular velocity exhibits the following relationship with the attitude of the robot $\eta = [\phi, \theta, \psi]^\top$ defined by ZYX Euler angle:

$$\omega = G_\eta \dot{\eta}, \quad (17)$$

$$G_\eta = \begin{bmatrix} 1 & 0 & -\sin\theta \\ 0 & \cos\phi & \cos\theta\sin\phi \\ 0 & -\sin\phi & \cos\theta\cos\phi \end{bmatrix}.$$

Moreover, $J(= \mathrm{diag}(J_1, J_2, J_3) \in R^{3\times3})$ is the inertia of the body; ψ is the yaw angle of the body; $\tau(= [\tau_1, \tau_2, \tau_3]^\top \in R^3)$ is the torque acting on the rigid body in the roll, pitch, and yaw directions; $\tau_d(= [\tau_{d1}, \tau_{d2}, \tau_{d3}]^\top)$ is the demanded torque; and $F(\omega)(= \omega \times J\omega)$ is the centrifugal Coriolis force.

In this study, the offset force f_o and offset torque τ_o are unknown parameters, whereas m and J are known. Note that the time constant T can be estimated from the preliminary experiment of wing performance described in Section 3.1. In the next section, a control law will be derived for the case where T is an unknown parameter as well.

5. CONTROLLER DESIGN

In this study, the control objectives are to maintain the attitude z to the target z_d and the altitude η of the robot body to the target η_d. Here, z_d and η_d are constant.

The offset force and torques in (10), (11), and (12) are unknown parameters included in the flight dynamics in (13) and (15). They are uncertain and cannot be measured. In this study, an adaptive estimation law is employed for these parameters.

5.1 Attitude Controller

Target of Angular Velocity First, from (17), the target angular velocity of the robot is designed as follows:

$$\omega_d = -G_\eta H e_\eta, \quad (18)$$

where $e_\eta = \eta - \eta_d$ and $H(= \mathrm{diag}(h_1, h_2, h_3))$ is a non-negative diagonal matrix. Furthermore, from (18), the higher-order derivatives

$$\dot{\omega}_d \approx -G_\eta H \dot{e}_\eta = -G_\eta H \dot{\eta},$$
$$\ddot{\omega}_d \approx -G_\eta H \ddot{e}_\eta = -G_\eta H \ddot{\eta},$$

are used. Note that, because the yaw motion of the robot cannot be controlled in this study, we set $h_3 = 0$.

Sliding Variable Second, we introduce the following sliding variable s_ω to achieve the target attitude:

$$s_\omega = \dot{e}_\omega + \Lambda_\omega e_\omega = \dot{\omega} - \dot{\omega}_r, \quad (19)$$

where $e_\omega(= \omega - \omega_d)$, $\dot{\omega}_r = \dot{\omega}_d - \Lambda_\omega(\omega - \omega_d)$, and $\Lambda_\omega(= \mathrm{diag}(\Lambda_{\omega1}, \Lambda_{\omega2}, \Lambda_{\omega3}))$ is a non-negative diagonal matrix. Note that, because the yaw motion of the robot cannot be controlled in this study, we set $\Lambda_{\omega3} = 0$.

Control Law Third, we consider the dynamics of the sliding variable s_ω. From (15), (16), and (19),

$$TJ\dot{s}_\omega = \tau_d - J\dot{\omega} - F - Y_\omega p_\omega \quad (20)$$

is derived. Here, the unknown parameter vector $p_\omega = [T, \tau_{o1}, \tau_{o2}, \tau_{o3}]^\top$, and a time-varying matrix Y_ω is given by

$$Y_\omega(\eta, \omega, \dot{\omega}; \Lambda_\omega, H) = \left[\dot{F} + J\ddot{\omega}_r,\ I_3\right].$$

For (20), by selecting the control input τ_d as

$$\tau_d = -K_\omega s_\omega + J\dot{\omega} + F + Y_\omega \hat{p}_\omega, \quad (21)$$

the dynamics in (20) is described by

$$TJ\dot{s}_\omega + K_\omega s_\omega = Y_\omega \tilde{p}_\omega, \quad (22)$$

where $\hat{p}_\omega$ is the estimate of p_ω, $\tilde{p}_\omega(= \hat{p}_\omega - p_\omega)$ is the error, and $K_\omega(= \mathrm{diag}(k_{\omega1}, k_{\omega2}, k_{\omega3}))$ is a non-negative diagonal matrix. Note that, because the yaw motion of the robot is not controlled in this study, $k_{\omega3} = 0$.

Adaptive Law The following Lyapunov function candidate is considered for (22):

$$V_\omega = \frac{1}{2}s_\omega^\top (TJ) s_\omega + \frac{1}{2}\tilde{p}_\omega^\top \Gamma_\omega^{-1} \tilde{p}_\omega, \quad (23)$$

where $\Gamma_\omega(= \mathrm{diag}(\gamma_{\omega1}, \cdots, \gamma_{\omega4})$ is an adaptive gain matrix with positive diagonal elements.

Considering (22), the time derivative of the Lyapunov function candidate in (23) is given by

$$\begin{aligned} \dot{V}_\omega &= s_\omega^\top (TJ\dot{s}_\omega) + \tilde{p}_\omega^\top \Gamma_\omega^{-1} \dot{\hat{p}}_\omega \\ &= s_\omega^\top \left(-K_\omega s_\omega + Y_\omega \tilde{p}_\omega\right) + \tilde{p}_\omega^\top \Gamma_\omega^{-1} \dot{\hat{p}}_\omega \\ &= -s_\omega^\top K_\omega s_\omega + s_\omega^\top Y_\omega \tilde{p}_\omega + \tilde{p}_\omega^\top \Gamma_\omega^{-1} \dot{\hat{p}}_\omega. \end{aligned} \quad (24)$$

For (24), by designing the adaptive law as

$$\dot{\hat{p}}_\omega = -\Gamma_\omega Y_\omega^\top s_\omega,$$

the time derivative in (24) becomes a negative definite:

$$\dot{V}_\omega = -s_\omega^\top K_\omega s_\omega \le 0.$$

As a result, the attitude control system is theoretically globally asymptotically stable according to the invariant set theorem.

5.2 Altitude Controller

The altitude controller is designed in a manner similar to that employed for the design of the attitude controller.

First, we introduce the following sliding variable s_z to control the altitude z to the target z_d:

$$\begin{aligned} s_z &= \ddot{e}_z + 2\lambda_z \dot{e}_z + \lambda_z^2 e_z \\ &= \ddot{z} + 2\lambda\dot{z} + \lambda_z^2 (z - z_d), \end{aligned} \quad (25)$$

where $e_z = z - z_d$ and λ_z is a positive value.

Second, considering (14) and (25), the time derivative of (13) is derived as follows:

$$T\dot{s}_z = \frac{f_d}{m} - \dddot{z} - g - Y_z p_z, \tag{26}$$

where the unknown parameter vector $p_z = [T, f_o]^\top$ and the time-varying matrix Y_z is given by

$$Y_z(\dot{z}, \ddot{z}; \lambda_z) = \left[-2\lambda\ddot{z} - \lambda_z^2\dot{z},\ \frac{1}{m}\right].$$

For (26), by selecting the control input f_d as

$$\frac{f_d}{m} = -k_z s_z + Y_z\hat{p}_z + \dddot{z} + g, \tag{27}$$

the dynamics in (26) is given by

$$T\dot{s}_z + k_z s_z = Y_z\tilde{p}_z, \tag{28}$$

where $\hat{p}_z$ is the estimate of p_z, $\tilde{p}_z(=\hat{p}_z - p_z)$ is the error, and k_z is a positive gain.

Third, the following Lyapunov function candidate is considered for (28):

$$V_z = \frac{T}{2}s_z^\top s_z + \frac{1}{2}\tilde{p}_z^\top\Gamma_z^{-1}\tilde{p}_z, \tag{29}$$

where $\Gamma_z(=\mathrm{diag}(\gamma_{z1}, \gamma_{z2}))$ is an adaptive gain matrix with positive diagonal elements.

Considering (28), the time derivative of the Lyapunov function candidate in (29) is given by

$$\begin{aligned}\dot{V}_z &= Ts_z^\top\dot{s}_z + \tilde{p}_z^\top\Gamma_z^{-1}\dot{\hat{p}}_z \\ &= s_z^\top(-k_z s_z + Y_z\tilde{p}_z) + \tilde{p}_z^\top\Gamma_z^{-1}\dot{\hat{p}}_z \\ &= -k_z s_z^\top s_z + s_z^\top Y_z\tilde{p}_z + \tilde{p}_z^\top\Gamma_z^{-1}\dot{\hat{p}}_z.\end{aligned} \tag{30}$$

For (30), by designing the adaptive law as

$$\dot{\hat{p}}_z = -\Gamma_z Y_z^\top s_z,$$

the time derivative in (30) becomes a negative definite:

$$\dot{V}_z = -k_z s_z^\top s_z \le 0.$$

As a result, the altitude control system is theoretically globally asymptotically stable according to the invariant set theorem.

5.3 Lift-force Demand and Voltage Amplitude

From the control inputs τ_d and f_d in (21) and (27) as well as the mixing matrix in (6), each lift-force demand is given by

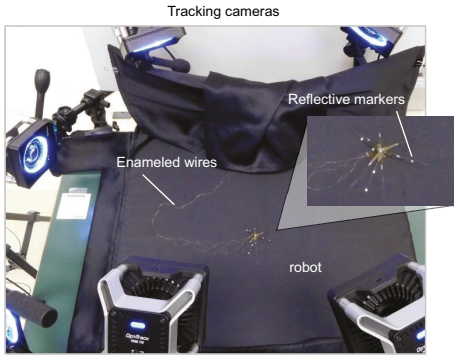

Fig. 8. Experimental system for tethered controlled flight.

$$\begin{bmatrix} f_{d,L} \\ f_{d,R} \\ f_{d,B} \end{bmatrix} = M^{-1}\begin{bmatrix} f_d \\ \tau_{d1} \\ \tau_{d2} \end{bmatrix}. \tag{31}$$

Consequently, for $i \in \{L, R, B\}$, each voltage amplitude V_i is calculated using (1) and (31).

6. EXPERIMENTS

The effectiveness of the proposed controller is demonstrated through a flight experiment.

6.1 Experimental Setting

Figure 8 shows our experimental system. Five markers are attached to the proposed flying robot, as shown in Fig. 1. The markers are tracked by a measurement system (OptiTrack Prime 17 W motion capture system), as shown in Fig. 8. Subsequently, a tracking personal computer (Intel Core i9-9900K, 8-core 3.6 GHz, 64 GB of RAM)

Fig. 9. Photographic sequence of a flight without control. Immediately after launch, the robot overturned.

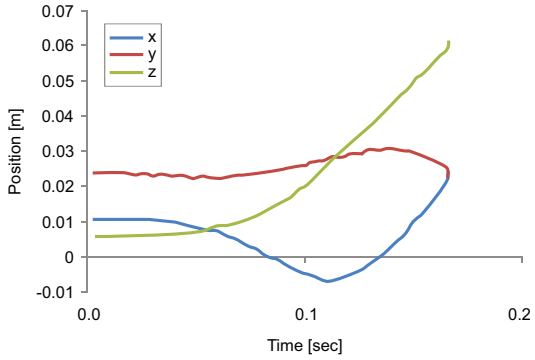

Fig. 10. Time series of the robot position during a flight at a constant voltage. Naturally, the robot was not controlled in the vertical direction, z.

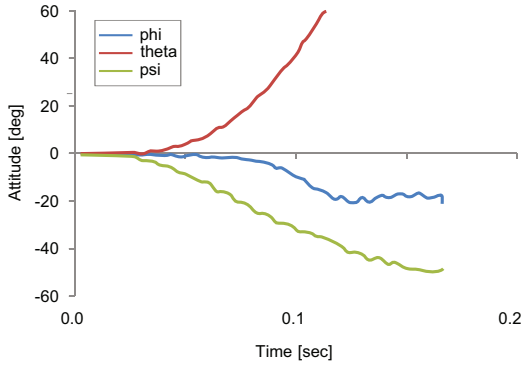

Fig. 11. Time series of the robot attitude during a flight at a constant voltage.

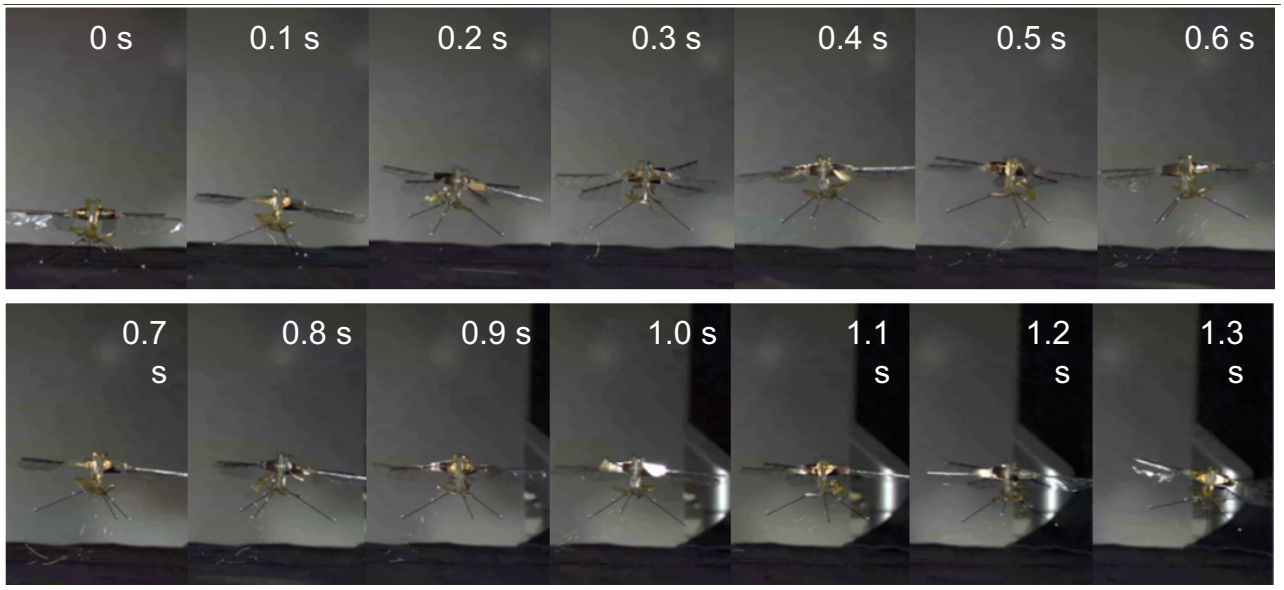

Fig. 12. Photographic sequence of a controlled flight.

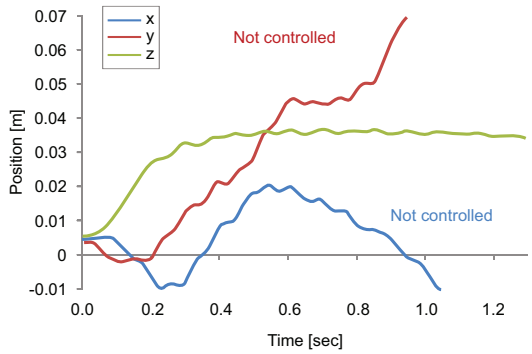

Fig. 13. Time series of the robot position during a controlled flight.

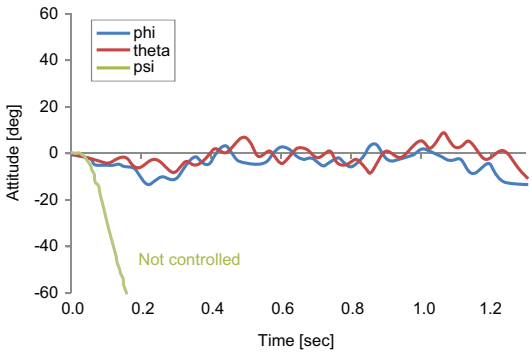

Fig. 14. Time series of the robot attitude during a controlled flight.

calculates the position and attitude of the robot and sends these values to a control personal computer (Intel Core i7-7700K, 4-core 4.2 GHz, 32 GB of RAM) in 3 ms. On using the control laws designed in section 5, each voltage amplitude is calculated. The amplitude is multiplied by the sinusoidal wave at 115 Hz produced by a function generator (Precision 4050B, B&K)using a multiplier (AD633, Analog Devices). Furthermore, the amplitude is amplified by 30 times with an amplifier (HJPZ-0.3P3, Matsusada Precision) and applied to the robot via enameled wires. Note that the same voltage amplitude is applied to paired wings to generate the same force.

6.2 Results

In the preliminary experiment, when the same voltages were applied to the three paired wings, the robot did not launch upward. Therefore, the calibration of the coefficients a_i and b_i in (1) is required. Figure 9 shows a photographic sequence of a flight without feedback control. The result is shown in Figs. 10 and 11. Owing to the application of constant voltage amplitudes greater than that required by the robot to support its own weight, the vertical position of the robot shifts upward. Furthermore, the roll and pitch angles could not remain near zero. In other words, it can be found that an offset torque exists owing to some misalignment to the lift forces. Finally, the robot stalled.

Figure 12 shows the result obtained with the proposed controller. Here, z_d and η_d are set to 0.04 and $[0, 0, 0]^\top$, respectively. After 0.06 s, the voltage amplitudes calculated by the proposed controller were applied. As shown in Fig. 13, the altitude z of the robot converged around the target z_d, although the steady-state error remained. In this study, the robot moved in the x and y directions gradually because the lateral position is not controlled. Figure 14 shows the attitude of the robot under control. As compared with Fig. 11, the robot could maintain the roll angle ϕ and pitch angle θ at around zero. Note that the proposed robot cannot control its yaw angle ψ.

7. CONCLUSION

A modeling and controller design for a newly developed flapping-wing robot with three paired actuators was pre-

sented in this study. The lift force generated by the paired-wing actuators was assumed to work at an acting point on spatio-temporal average. The modeling error was defined by the misalignment of the force frame related to the body frame, and unknown parameters were derived as the offset force and torques. Furthermore, an adaptive law was employed because these parameters cannot be measured. Finally, tethered controlled flight was demonstrated, and the proposed controller enabled the robot to control its altitude and attitude.

Future work will involve the construction of a lateral controller for hovering. Considering the requirement for preliminary calibration of the lift-force model in (1), it may be desirable to control each voltage amplitude for the paired wings directly using an adaptive rule. Furthermore, toward the untethered flight of an FW-MAV weighing a few grams including a battery, highly efficient booster and lightweight electrical control circuits will be required. The integration of these circuits, battery, sensor unit, and online computation is another important future task.

ACKNOWLEDGEMENTS

The authors would like to thank Dr. Kanae Hamaguchi and Norikazu Ohta from Toyota Central R&D Labs, Inc. for their work regarding the hardware design and development.

REFERENCES

Azhar, M., Campolo, D., Lau, G.K., Hines, L., and Sitti, M. (2013). Flapping wings via direct-driving by dc motors. *Proceedings of IEEE International Conference on Robotics and Automation (ICRA)*, 1397–1402.

Bronson, J.R., Pulskamp, J.S., Polcawich, R.G., Kroninger, C.M., and Wetzel, E.D. (2009). PZT MEMS actuated flapping wings for insect-inspired robotics. *Proceedings of 22nd IEEE International Conference on Micro Electro Mechanical Systems*, 1047–1050.

Chirarattananon, P., Ma, K.Y., and Wood, R.J. (2013). Adaptive control for takeoff, hovering, and landing of a robotic fly. *Proceedings of IEEE/RSJ International Conference on Intelligent Robots and Systems (IROS)*.

de Croon, G.C.H.E., de Clercq, K.M.E., Ruijsink, R., Remes, B., and de Wagter, C. (2009). Design, aerodynamics, and vision-based control of the DelFly. *International Journal of Micro Air Vehicles*, 1(2), 71–97.

Dickinson, M.H., Lehmann, F.O., and Sane, S.P. (1999). Wing rotation and the aerodynamic basis of insect flight. *Science*, 284, 1954–1960.

Hines, L., Campolo, D., and Sitti, M. (2014). Liftoff of a motor-driven, flapping-wing microaerial vehicle capable of resonance. *IEEE Transactions on Robotics*, 30(1), 220–232.

Keennon, M., Klingebiel, K., Won, H., and Andriukov, A. (2012). Development of the nano hummingbird: A tailless flapping wing micro air vehicle. *Proceedings on 50th AIAA Aerosp. Sci. Meeting Including New Horizons Forum Aerosp.*, 1–24.

Ma, K.Y., Chirarattananon, P., Fuller, S.B., and Wood, R.J. (2013). Controlled flight of a biologically inspired, insect-scale robot. *Science*, 340(6132), 603–607.

Mateti, K., Byrne-Dugan, R.A., Tadigadapa, S.A., and Rahn, C.D. (2012). Wing rotation and lift in SUEX flapping wing mechanisms. *Smart Materials and Structures*, 22(1), 014006.

Nguyen, V.Q., Syaifuddin, M., Park, H.C., D. Y. Byun, N.S.G., and Yoon, K.J. (2008). Characteristics of an insect-mimicking flapping system actuated by a unimorph piezoceramic actuator. *Journal of Intelligent Material Systems and Structures*, 19(10), 1185–1193.

Orlowski, C.T. and Girard, A.R. (2012). Dynamics, stability, and control analyses of flapping wing micro-air vehicles. *Progress in Aerospace Sciences*, 51, 18–30.

Ozaki, T. and Hamaguchi, K. (2018a). Bioinspired flapping-wing robot with direct-driven piezoelectric actuation and its takeoff demonstration. *IEEE Robotics and Automation Letters*, 3(4), 4217–4224.

Ozaki, T. and Hamaguchi, K. (2018b). Electro-aeromechanical model of piezoelectric direct-driven flapping-wing actuator. *Applied Sciences*, 8(9), 1699.

Ozaki, T. and Hamaguchi, K. (2018c). Performance of direct-driven flapping-wing actuator with piezoelectric single-crystal PIN-PMN-PT. *Journal of Micromechanics and Microengineering*, 28.

Wood, R.J. (2008). The first takeoff of a biologically inspired at-scale robotic insect. *IEEE Transactions on Robotics*, 24(2), 341–347.

Zhang, J., Fei, F., Tu, Z., and Deng, X. (2017). Design optimization and system integration of robotic hummingbird. *Proceedings on IEEE International Conference on Robotics and Automation (ICRA)*, 5422–5428.